Transition to complex dynamics in the cubic lid-driven cavity

Juan M. Lopez,* Bruno D. Welfert, Ke Wu, and Jason Yalim
School of Mathematical and Statistical Sciences, Arizona State University, Tempe, Arizona 85287, USA
(Received 10 March 2017; published 12 July 2017)

The onset of time dependence in the cubic lid-driven cavity is surprisingly complicated, given the simplicity of the geometry and the modest value of the Reynolds number at which it occurs. The onset is characterized by finite-amplitude oscillations that appear to be stable for long times, but are subjected to intermittent bursts at irregular times during which the reflection symmetry about the spanwise midplane is broken. The complex dynamics are shown to be intimately related to the subcritical nature of the instability of the steady basic state. We use a spectral collocation numerical technique, solving both in the full three-dimensional space and in the symmetric subspace, and use selective frequency damping and Arnoldi iterations about the unstable basic state to determine its bifurcations. Edge tracking is also used to investigate a number of time-dependent saddle states. Putting all this together, we show that the complex dynamics are organized by two successive Hopf bifurcations, the first of which is shown to be subcritical. All local states are unstable in the full space at higher Reynolds numbers, leading to the intermittent bursting behavior.

DOI: 10.1103/PhysRevFluids.2.074401

I. INTRODUCTION

Lid-driven cavity flow, consisting of the flow in a rectangular cavity driven by the steady translation of one of the cavity walls, is a canonical flow for the study of the stability of separated shear layers. The idealized situation where the cavity is of infinite spanwise extent and the flow is assumed to be invariant in the spanwise direction has been studied extensively; see the review article by Shankar and Deshpande [1].

In the cubic cavity, the spanwise confinement effects are pronounced, and for Reynolds numbers $\mathrm{Re} \sim 10^3$, the flow is steady with a single pair of streamwise vortices centered about the spanwise midplane, together with vortical structures along the edges where the spanwise walls meet the other walls. When the Reynolds number is increased beyond approximately 1910, the flow becomes unsteady, manifesting long periods of essentially periodic flow with intermittent bursts, and for slightly larger Re, the flow is persistently chaotic. A number of numerical investigations have contributed to the details of the flow dynamics in this regime where the flow in the cubic lid-driven cavity becomes unsteady. In the earliest such study, Feldman and Gelfgat [2] report that the steady flow loses stability at a subcritical Hopf bifurcation, with unsteady flow appearing for $\mathrm{Re} \gtrsim 1914$. The more recent studies of Kuhlmann and Albensoeder [3], Loiseau [4], and Loiseau et al. [5] reproduce some aspects of the flows reported by Feldman and Gelfgat [2], but note that the periodic state of [2] is not stable beyond the Hopf bifurcation and that it undergoes sudden bursts at random times. They conclude that the simulations of [2] were not run long enough for the intermittent bursts to manifest; near onset, it takes several viscous times for this to happen. Also, near onset the intervals between bursts can be very long (several viscous times). Following a burst, another essentially periodic state with larger amplitude and smaller frequency that persists for a relatively short time is observed before another burst occurs. The dynamics involved remain unclear; Ref. [4] suggests that it is some type of intermittency that requires further investigation to unravel, Ref. [3] calls for further investigations to clarify the situation, and Ref. [5] concludes that the origin of the intermittent events is still unknown. The numerical studies each use very different methods with

*jmlopez@asu.edu

a wide range of spatial and temporal resolutions; Ref. [2] uses finite differences, Ref. [3] uses Chebyshev spectral collocation, and Refs. [4,5] use spectral elements. The results from the spectral collocation and the spectral element methods, which were run for sufficiently long times, are in agreement. There are minor variations in the precise value of Re at which things happen, but this is readily accounted for by differences in resolution and the treatment of the discontinuous boundary condition at the edges where the moving lid meets the stationary walls. Thus, the transition from steady flow to intermittent bursting when Re is increased beyond a critical value is consistently observed by the various computations. The only experiment specifically designed to address this onset of unsteady flow in the lid-driven cube [6] is broadly consistent with the numerical results, but the resolution in Re available in the experiment was insufficient to resolve the details.

Linear stability analyses of the types so far employed have been incapable of capturing the nature of the onset of the intermittent bursting reported from nonlinear simulations in the cubic cavity. In part, the problem is that linear stability analysis only gives the eigenstructure near instability, and for the cubic lid-driven cavity, the studies all agree that instability is via a subcritical Hopf bifurcation. Since the bifurcation is subcritical, the subsequent flow evolution is not well described by the bifurcating eigenmode. The previous nonlinear studies of the cubic cavity flow all report that the reflection symmetry about the spanwise midplane is broken to some degree in the unsteady nonlinear states, but they do not provide details about the nature of this symmetry breaking nor how it is related to the onset of unsteadiness.

Here we use a Chebyshev spectral collocation method, similar in many ways to that used in [3] but with a different treatment of the boundary condition discontinuity, and our nonlinear results are in very close agreement with [3–5]. By computing in both the full three-dimensional space and the reflection-symmetric subspace, we are able to show that the second periodic oscillations that are observed briefly following the bursts in fact correspond to a limit cycle that is unstable to symmetry breaking and exist for much lower Re than that at which the basic state first loses stability. As was done in [4,5], we also compute the unstable basic state via selective frequency damping [7] and then use Arnoldi iterations [8] to study its linear stability. In agreement with [4,5], the limit cycle reported in [2] corresponds to the first pair of complex-conjugate eigenvalues to acquire a positive real part as Re is increased. As noted in [2,3], this Hopf bifurcation is subcritical and we reconfirm this by computing the lower branch down to the cyclic-fold bifurcation at lower Re $\approx$ 1872 using an edge state technique (EST) [9,10]. We have also located a second Hopf bifurcation at Re $\approx$ 2089 whose eigenfrequency is very close to that of the intermittent large-amplitude oscillations that are observed following a burst in the nonlinear simulations. This was also noted by Loiseau *et al.* [4,5], but they did not study the linear stability of the basic state beyond Re $=$ 2000 and so missed this second bifurcation. By monitoring the symmetry of the nonlinear solutions, it is clear that the large-amplitude oscillations immediately following a burst are unstable to symmetry breaking. So we have also computed the nonlinear solutions in the symmetry subspace and indeed found that these large-amplitude oscillations correspond to a limit cycle solution. We have continued this limit cycle down to much lower Re $\approx$ 1872 where it undergoes a cyclic-fold bifurcation. Then, using the EST in the symmetric subspace with combinations of the limit cycle and the basic state as initial conditions, we have been able to capture the details of the lower-branch saddle limit cycle for a small range in Re. The lower-branch limit cycle undergoes a Neimark-Sacker bifurcation and acquires two unstable directions, thus compromising the effectiveness of the EST to track it. However, at the Neimark-Sacker bifurcation, a quasiperiodic state is spawned that has one unstable direction in the symmetry subspace. We have tracked this state using the EST to slightly higher Re where it is absorbed in a subcritical Neimark-Sacker bifurcation of the upper branch of the other (low-amplitude) limit cycle, rendering that limit cycle unstable. By taking the various edge states computed in the symmetry subspace as initial conditions for nonlinear simulations in the full space, we have also been able to extract crucial information about which states are unstable to symmetry breaking. By piecing all this information together, we are able to provide a fairly complete and consistent picture of what is responsible for the bursting behavior.

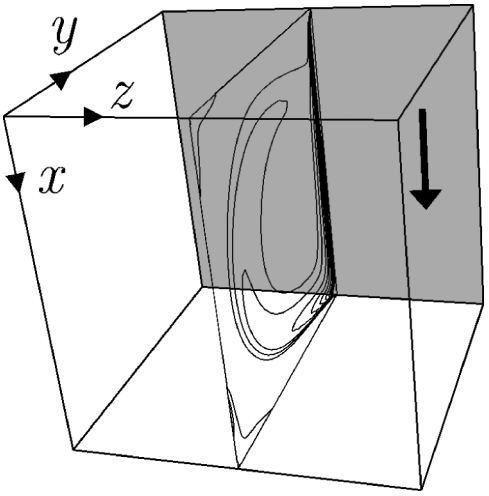

FIG. 1. Schematic of the cubic lid-driven cavity. The perspective shown, with the back wall (at $y = 0.5$, shaded gray) moving downward ($+x$ direction), is that used in all subsequent three-dimensional renderings of the results. In the spanwise midplane (at $z = 0$), typical streamlines of a low-Re steady-state flow are shown.

II. GOVERNING EQUATIONS AND NUMERICAL TECHNIQUES

Consider the flow in a cube of sides of length L, completely filled with an incompressible fluid of kinematic viscosity ν, driven by the motion of one wall at constant velocity U. Using L as the length scale and L/U as the time scale, the nondimensional governing equations are

$$\partial \boldsymbol{u}/\partial t + \boldsymbol{u} \cdot \boldsymbol{\nabla} \boldsymbol{u} = -\boldsymbol{\nabla} p + \mathrm{Re}^{-1} \nabla^2 \boldsymbol{u}, \quad \boldsymbol{\nabla} \cdot \boldsymbol{u} = 0, \tag{1}$$

where the Reynolds number

$$\mathrm{Re} = UL/\nu \tag{2}$$

is the ratio of two time scales: the viscous time scale L^2/ν and the convective time scale L/U. For the most part, we will present results using the convective time scale, but the time series of flow quantities will be shown in terms of the viscous time scale. As such, we introduce $\tau = t/\mathrm{Re}$, where one time unit in τ is a viscous time.

The Cartesian coordinate system $\boldsymbol{x} = (x,y,z)$ with the origin at the center of the cube is used; x is the direction in which the wall at $y = 0.5$ is moving, z is the spanwise direction, and the velocity field is $\boldsymbol{u} = (u,v,w)$. See Fig. 1 for a schematic.

The boundary conditions on the stationary walls at $x = \pm 0.5$, $y = -0.5$, and $z = \pm 0.5$ are no slip, i.e., $\boldsymbol{u} = \boldsymbol{0}$ on these walls. Nominally, on the moving wall $(u,v,w) = (1,0,0)$, resulting in a jump discontinuity along the four edges, $(x,y,z) = (\pm 0.5, 0.5, z)$ and $(x, 0.5, \pm 0.5)$, where the moving wall meets the streamwise and spanwise walls.

The system (1), together with the boundary conditions, is equivariant with respect to a reflection symmetry $\mathcal{K}$ about the spanwise midplane $z = 0$. The action of this Z_2 symmetry on the velocity, vorticity $\boldsymbol{\nabla} \times \boldsymbol{u} = (\xi,\eta,\zeta)$, and helicity $\mathcal{H} = \boldsymbol{u} \cdot (\boldsymbol{\nabla} \times \boldsymbol{u})$ is

$$\mathcal{A}(\mathcal{K})(u,v,w)(x,y,z) = (u,v,-w)(x,y,-z), \tag{3a}$$

$$\mathcal{A}(\mathcal{K})(\xi,\eta,\zeta)(x,y,z) = (-\xi,-\eta,\zeta)(x,y,-z), \tag{3b}$$

$$\mathcal{A}(\mathcal{K})\mathcal{H}(x,y,z) = -\mathcal{H}(x,y,-z). \tag{3c}$$

The flow in the cubic lid-driven cavity is inherently three dimensional for all Re $\neq 0$. It is interesting to visualize the flow in terms of the helicity, which for the idealized spanwise invariant case is identically zero since the velocity and vorticity vectors are orthogonal.

A convenient global measure of the flow is the kinetic energy

$$E = \frac{1}{2}\int_{\mathcal{C}} |\boldsymbol{u}|^2 d\boldsymbol{x}, \tag{4}$$

where $\mathcal{C}$ is $\boldsymbol{x} \in [-0.5,0.5] \times [-0.5,0.5] \times [-0.5,0.5]$. It is also convenient to introduce a symmetry parameter in order to measure the relative departure from symmetry of a solution:

$$S = \frac{1}{2E}\int_{\mathcal{C}} |\boldsymbol{u} - \mathcal{A}(\mathcal{K})\boldsymbol{u}|^2 d\boldsymbol{x}. \tag{5}$$

This symmetry parameter is proportional to the kinetic energy in the skew-symmetric component of the flow relative to the total kinetic energy of the flow.

Numerics

The Navier-Stokes system (1) is discretized using a spectral-collocation method in all spatial directions. Both velocity and pressure are approximated by polynomials of degree N ($\mathcal{P}_N$ and $\mathcal{P}_N$), written in barycentric form with weights $w_0 = 0.5$, $w_n = (-1)^n$ for $n \in [1, N-1]$, and $w_N = 0.5(-1)^N$, associated with the Chebyshev-Gauss-Lobatto grid. Spatial differentiation is performed via direct matrix-vector multiplication by the pseudospectral differentiation matrix (common to all three directions).

The time integration scheme used is the fractional-step improved projection method of Hugues and Randriamampianina [11], based on a linearly implicit and stiffly stable, second-order accurate scheme combining a backward differentiation formula for the linear terms and an explicit mix, equivalent to linear extrapolation, of Adams-Moulton and Adams-Bashforth steps for the nonlinear convective terms [12]. The predictor stage of the fractional step method solves a Helmholtz equation for a pressure field, for which Neumann conditions consistent with (1) are applied at the walls. The corrector stage then projects the resulting predicted velocity field onto the space of (discretely) divergence-free polynomials via a Stokes problem, which is also handled by solving a Helmholtz equation for the corrected pressure, albeit with homogeneous Neumann boundary conditions. Further details can be found in [11].

The boundary condition for the streamwise component of velocity for the moving wall, $u = 1$, is discontinuous where it meets the four stationary walls. Discontinuous boundary conditions can lead to numerical problems when using spectral methods and so we regularized it by using

$$u(x,0.5,z) = \left[1 - 2\exp\left(\frac{-1}{\epsilon}\right)\cosh\left(\frac{2x}{\epsilon}\right)\right]\left[1 - 2\exp\left(\frac{-1}{\epsilon}\right)\cosh\left(\frac{2z}{\epsilon}\right)\right]. \tag{6}$$

The small positive number ϵ controls the distance over which the discontinuity is smoothed. This is a standard technique used in spectral methods [13]. As ϵ is decreased for a given Re, the accuracy of the spectral method becomes dominated by the need to resolve the steep variation in (6) rather than the flow. For the results presented here, with Re $\leqslant 2100$, we have used $\epsilon = 0.01$, for which $N = 48$ is sufficient to resolve (6), having five collocation points in the gap. When using local methods, such as finite-difference and finite-volume techniques, the gap is the grid spacing at the edge, so the gap decreases as the resolution is increased. An alternative treatment for global spectral methods is to try to account for the discontinuity asymptotically [14]. Kuhlmann and Albensoeder [3] implemented such an approach, but were unable to account for the discontinuity at the four corners where the edges meet, $(x,y,z) = (\pm 0.5, 0.5, \pm 0.5)$. They noted that their spectral accuracy was considerably reduced as a consequence. The size of the gap has a direct impact on, for example, the critical Re for the onset of instability; a smaller gap results in a smaller critical Re_{H1}. In their finite-volume study, Feldman and Gelfgat [2] found by direct simulation that for their highest resolution (and hence their smallest

gap), the basic state loses stability via a subcritical Hopf bifurcation H_1 at $\mathrm{Re} = \mathrm{Re}_{H1} \approx 1927$. This compares very well with $\mathrm{Re}_{H1} \approx 1929$ that we find using $\epsilon = 0.01$ and $N = 48$. They then used Richardson extrapolation to estimate $\mathrm{Re}_{H1} = 1914$. Kuhlmann and Albensoeder [3] report $\mathrm{Re}_{H1} \approx 1920$ using $N = 72$, although their $N = 48$ result is very close ($\approx$1918). With all of this under consideration, our choice of ϵ represents a 1% gap along the edges and about a 0.5% increase in Re_{H1} over what it would be with a zero gap. This allows us to have good spectral resolution with a relatively modest $N = 48$. In the following sections, we demonstrate excellent agreement with the previous numerical studies of the cubic lid-driven cavity. Small quantitative differences correspond to small shifts in the given Re due to the gap size differences. Most importantly, the details of the intermittent bursts for $\mathrm{Re} > \mathrm{Re}_{H1}$ that we find are in agreement with those reported in [3–5].

For $\mathrm{Re} < \mathrm{Re}_{H1} \approx 1929$ the stable basic state (BS) can be determined via direct numerical simulation (DNS). At $\mathrm{Re} = \mathrm{Re}_{H1}$, the BS loses stability via a (subcritical) Hopf bifurcation and cannot be computed via DNS. However, it can be computed by introducing a feedback control $\boldsymbol{v}$ into (1) and using the selective frequency damping (SFD) technique described in [7]. Specifically, we solve the augmented system

$$\partial \boldsymbol{u}/\partial t + \boldsymbol{u} \cdot \nabla \boldsymbol{u} = -\nabla p + \mathrm{Re}^{-1} \nabla^2 \boldsymbol{u} + \omega_c (\boldsymbol{v} - \boldsymbol{u}), \tag{7a}$$

$$\partial \boldsymbol{v}/\partial t = \omega_c (\boldsymbol{u} - \boldsymbol{v}), \quad \nabla \cdot \boldsymbol{u} = 0, \quad \nabla \cdot \boldsymbol{v} = 0, \tag{7b}$$

with $\boldsymbol{v} = \boldsymbol{u}$ on all boundaries. Equation (7b) represents a low-pass filter applied to $\boldsymbol{u}$, with cutoff frequency ω_c. The selection $\omega_c = \omega/2$ optimizes damping of unstable modes of (7) oscillating at a target frequency ω close to the Hopf frequency associated with H_1. The velocity and feedback control fields $\boldsymbol{u}$ and $\boldsymbol{v}$ are (pseudo)spectrally collocated and (7) is solved using the same technique as that used for (1). In the time-splitting scheme, the high-frequency term $\omega_c(\boldsymbol{v} - \boldsymbol{u})$ in (7a) is treated implicitly, while $\omega_c(\boldsymbol{u} - \boldsymbol{v})$ in (7b) is treated as a nonlinear term, using linear extrapolation.

The linear stability of the unstable BS found via SFD is analyzed using a standard Arnoldi iteration [8] applied in two different ways. In one, the Navier-Stokes equations are linearized around the BS and subjected to a small perturbation [15]. In the other implementation, the action of the Jacobian is approximated with a divided difference constructed from the full nonlinear flow (1), evaluated at the BS in the direction of the small perturbation, as described in [16]. In both implementations, the corresponding Krylov subspaces consist of $m = 96$ modes. Each mode is obtained using 1000 time steps in a time window of 2×10^{-3} viscous times, guaranteeing a sufficiently high Nyquist frequency to accurately resolve the frequencies of interest while avoiding aliasing effects for this choice of m. The nonlinear implementation has an additional time window constraint due to nonlinear growth effects, but allows the original DNS solver to be used with only minor modifications. With the time window and m used, both implementations give comparable results.

III. RESULTS

A. Onset of unsteadiness

The flow in the cubic lid-driven cavity for sufficiently small Re is steady and symmetric. This BS has been shown to be stable for $\mathrm{Re} \lesssim 1900$ [2–5]. We find that for $\mathrm{Re} \lesssim 1929$, static continuation converges to the stable BS. However, for $\mathrm{Re} = 1930$, using the BS at $\mathrm{Re} = 1929$ as the initial condition, the evolution does not converge to a steady state. There is an initial adjustment to a state that is very similar to the BS and then over a long time (several viscous time units) there are small oscillations about the BS that are slowly amplified. These oscillations are damped for $\mathrm{Re} \lesssim 1929 \approx \mathrm{Re}_{H1}$. Similar behavior was reported in [2], which found $\mathrm{Re}_{H1} = 1927$ from direct simulations.

Figure 2(a) shows the temporal evolution of both the kinetic energy E and the symmetry parameter S in the $\mathrm{Re} = 1930$ case, using the BS at $\mathrm{Re} = 1929$ as the initial condition. Note that we plot all time series with respect to the viscous time τ. During the early evolution ($\tau \lesssim 4$), the flow consists of very slowly amplified oscillations about the unstable BS, during which time the flow is symmetric,

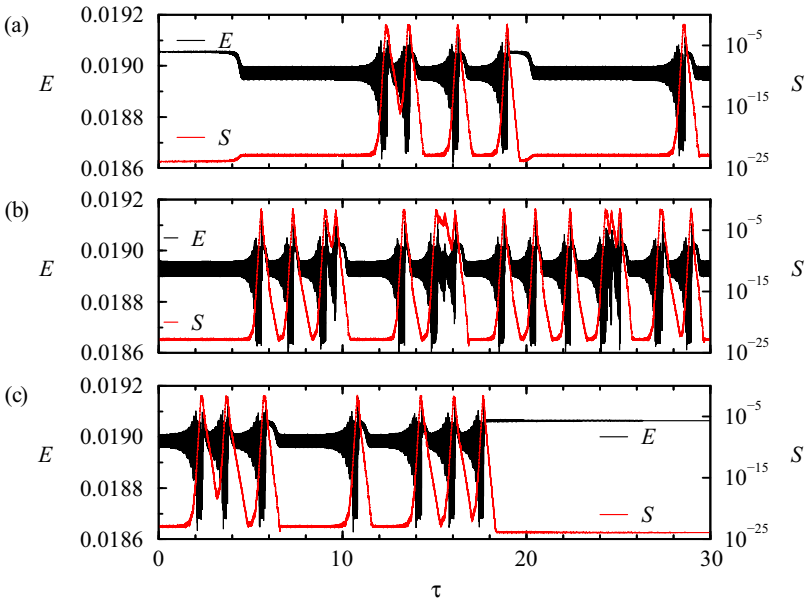

FIG. 2. Time series of E (black) and S (red) for (a) Re = 1930, (b) Re = 1940, and (c) Re = 1927.

as indicated by $S \sim 10^{-24}$, which is essentially machine epsilon squared. Then for $\tau \in (4,4.5)$, there is a rapid evolution away from the unstable BS, and by $\tau \approx 5$, the flow appears to have settled into a periodic limit cycle state, called LC1. There is a very slight increase in S from about 10^{-24} to 10^{-23}, but this level is still very close to being essentially zero. For a very long time (up to $\tau \sim 11$), it appears that LC1 is a stable symmetric limit cycle state. This behavior was also reported in [2], but as pointed out in [3], LC1 is unstable for $\mathrm{Re} > \mathrm{Re}_{H1}$. By $\tau \approx 11$, there is a rapid exponential growth in S, accompanied by rapidly growing oscillations in E that saturate at $\tau \approx 12$ to what appears to be another limit cycle LC2, and S has nonlinearly saturated to a level of order 0.01. The LC2 state persists for a very short time, about ten oscillations or 0.2 viscous times, after which the flow evolves back toward LC1 with S decaying exponentially. A sequence of bursts, during which S grows exponentially again, then occurs. At about $\tau = 19$, Fig. 2(a) shows that following another burst, the flow evolves very close to the BS and then settles near LC1 for several viscous times before executing another burst visiting LC2 and the BS.

The timing between the bursts is not uniform. This intermittent bursting behavior has been reported in [3–5] and all studies note that the flow is essentially symmetric when near the unstable BS and LC1 states and the broken symmetry is only strongly evident while it is near the LC2 state. None of the studies were able to determine the nature of the intermittency in the bursting behavior, but noted that the bursts become more frequent with increased Re, with the time intervals between bursts remaining irregular. Figure 2(b) shows a time series of E and S of the bursting state at Re = 1940, when started from the bursting state at Re = 1930.

For $\mathrm{Re} < \mathrm{Re}_{H1}$, evolutions starting from a bursting state at higher Re eventually tend to converge to the BS. Figure 2(c) shows the evolution of E and S for Re = 1927 starting again from the bursting state at Re = 1930. The flow continues to burst for a long time (approximately 18 viscous times) before an excursion visiting the phase-space neighborhood of the BS. Since the BS is stable at Re = 1927, it ends up attracting the flow.

During the time that the flow is evolving close to LC1 or LC2, one is able to characterize these two unstable limit cycles. Figure 3 shows snippets of the time series of E at Re = 1930, taken from Fig. 2(a) at times when the flow is evolving close to either LC1 or LC2. The time origin in this figure has been shifted so as to directly compare the energy evolutions. The amplitude and period

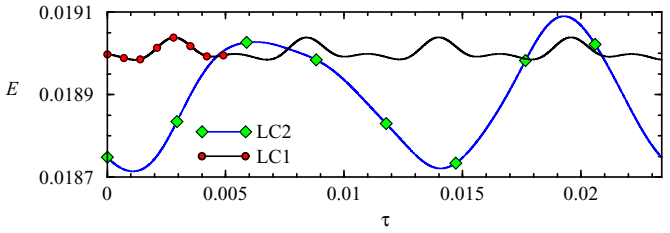

FIG. 3. Time series of E for LC1 and LC2 at Re $= 1930$; the symbols correspond to the snapshots over one period shown in Figs. 4 and 5.

of the oscillation of LC2 are about four times those of LC1. Specifically, the period ratio of LC2 to LC1 at Re $= 1930$ is 4.18, which is very close to the values reported in [3–5]. Also, the oscillations associated with LC1 and LC2 are very nonlinear, even though the value of Re is very close to Re_{H1} where the BS loses stability.

To better identify the flow features associated with the unsteadiness in LC1 and LC2, we consider the deviations away from their mean. Figures 4 and 5 show ten snapshots over one period of the deviation in the helicity, $\mathcal{H} - \langle\mathcal{H}\rangle$, for LC1 and LC2, respectively, where $\langle\cdot\rangle$ denotes the time average over one period. The deviations are of comparable strength to the means; these are not small perturbations about the mean. For both limit cycles, the deviation is associated with the streamwise vortices; the helicity associated with the spanwise end-wall regions remains essentially steady throughout the oscillations. For both limit cycles, the deviations are $\mathcal{K}$ symmetric, but the details differ for the two. For LC1, the deviation rollers for the most part remain in their spanwise location, but progressively change their sign through the cycle. In contrast, the deviation rollers of LC2 travel in from the spanwise end walls and annihilate at the midplane $z = 0$ as new rollers are spawned at the spanwise end walls, much like left- and right-traveling waves meeting at the $z = 0$

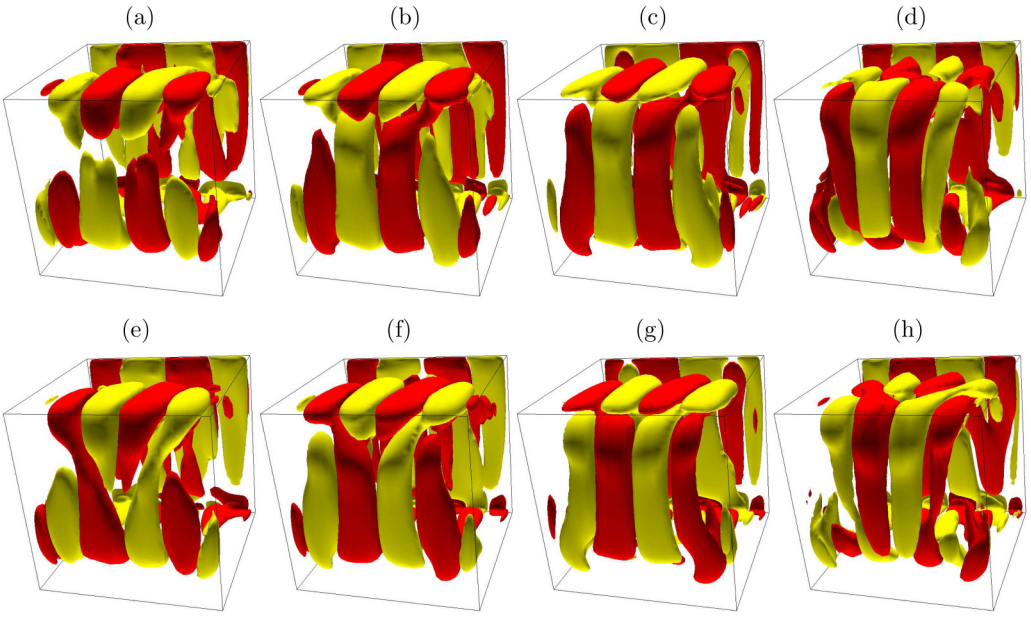

FIG. 4. Isosurfaces of $\mathcal{H} - \langle\mathcal{H}\rangle$ at $\pm 10^5$ of LC1 at Re $= 1930$, over one period $T = 10.8$ (convective time units). See movie 1 in the Supplemental Material [17] for an animation. (a) $t = 0$, (b) $T/8$, (c) $2T/8$, (d) $3T/8$, (e) $4T/8$, (f) $5T/8$, (g) $6T/8$, and (h) $7T/8$.

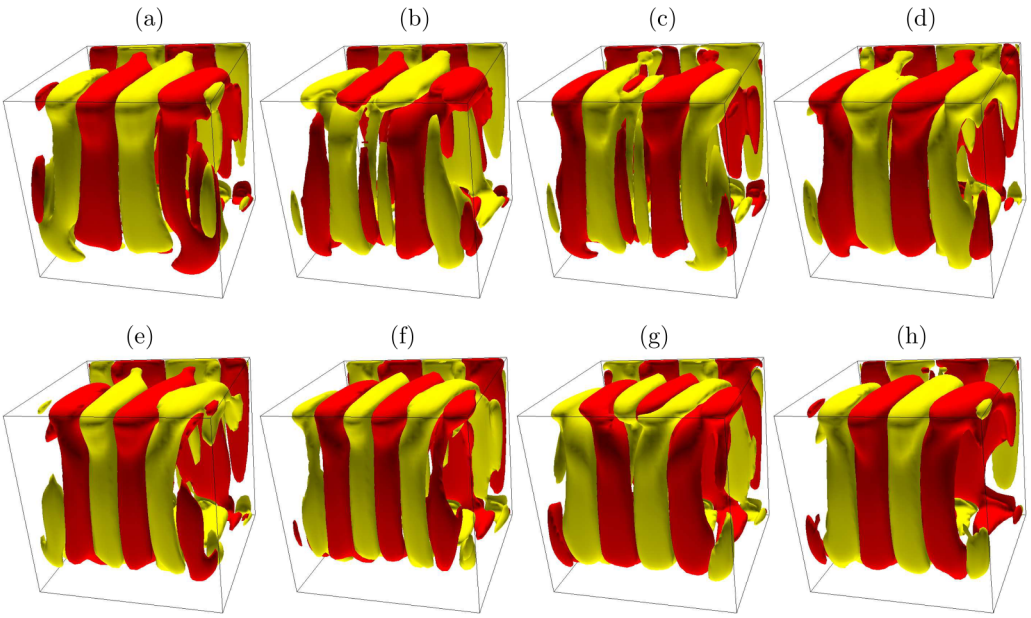

FIG. 5. Isosurfaces of $\mathcal{H} - \langle\mathcal{H}\rangle$ at $\pm 10^5$ of LC2 at Re $= 1930$, over one period $T = 45.2$ (convective time units). See movie 2 in the Supplemental Material [17] for an animation. (a) $t = 0$, (b) $T/8$, (c) $2T/8$, (d) $3T/8$, (e) $4T/8$, (f) $5T/8$, (g) $6T/8$, and (h) $7T/8$.

midplane. These flows are represented in the snapshots shown in Figs. 4 and 5, but the associated online movies 1 and 2 [17] provide a much clearer picture of their spatiotemporal features.

B. Intermittent bursting

Figure 6 shows time series of E and S for a number of cases with Re $\geqslant 1970$, where the flow is much more irregular with many excursions away from and back toward the symmetry subspace (exponential decay and growth in S). The approaches to either the BS or LC1 occur much less frequently than for the lower Re cases shown in Fig. 2. The bursts at these higher Re are occasionally into the symmetry subspace for a very brief period, rather than what was happening at lower Re, with the bursts providing short-lived excursions out of the subspace. Also, the excursions are not visiting the BS, LC1, or LC2 very often, but instead appear to be visiting quasiperiodic states and more complicated states, such as chaotic saddles.

The evolution at Re $= 1980$ shown in Fig. 6(b) has regular oscillations for $\tau \in (19,20)$ that do not correspond to either LC1 or LC2. Figure 7(a) shows details of the E and S time series over this time. The quasiperiodic oscillation is close to being periodic; this is indicated by the low beat frequency modulating the signal. The power spectral density of the E time series over the time shown in Fig. 7(a) is presented in Fig. 7(b), which consists of peaks at the frequencies corresponding to the two limit cycles LC1 and LC2 (ω_1 and ω_2, respectively) plus linear combinations of these. Also evident is a very-low-frequency peak corresponding to the beat frequency noticeable in the time series, which also shows up as sidebands to the main peaks. The frequencies ω_1 and ω_2 are close to a 4:1 ratio and the beat frequency is a measure of how far the ratio is from being rational. In Fig. 6(a), the time series for Re $= 1970$ also shows that the flow is close to this quasiperiodic mixed-mode QPa during $\tau \in (26.4,27.5)$.

At larger Re $= 2000$, the flow continues being spatiotemporally complicated. The chaotic behavior is similar to that reported in [4]. However, careful inspection reveals episodes of "orderly" bursts, as illustrated in Fig. 8, where at $\tau \approx 12.2$ the flow is very close to the BS and then it evolves close to LC1, during which time S is decreasing exponentially to very small values. Then,

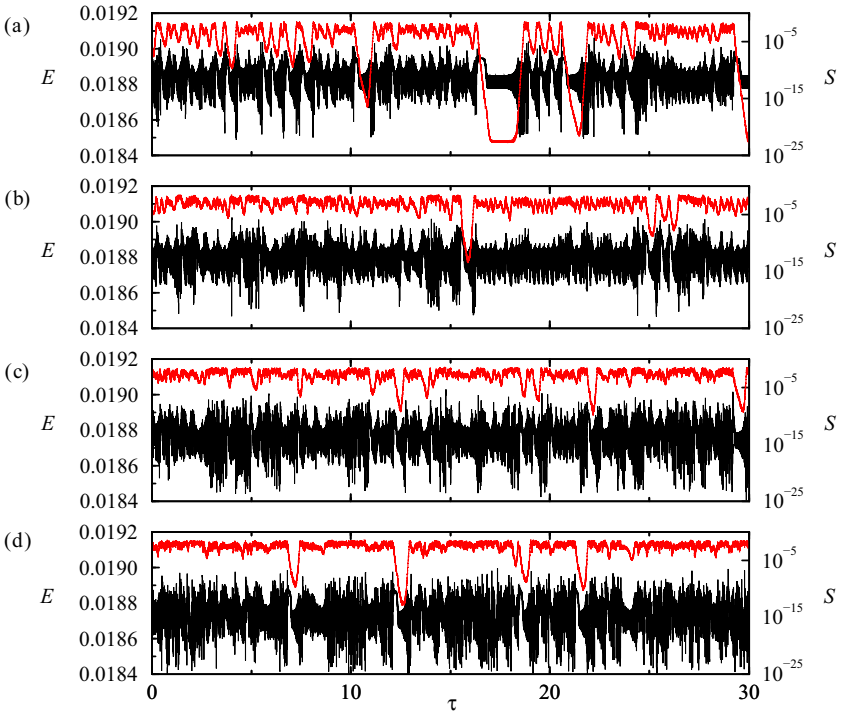

FIG. 6. Time series of E (black) and S (red) at (a) Re = 1970, (b) Re = 1980, (c) Re = 1990, and (d) Re = 2000.

at $\tau \approx 12.6$, the flow evolves away from LC1 to the mixed-mode QPa with S increasing; QPa gives way to LC2 at $\tau \approx 12.9$ for two or three cycles by which time S has saturated. Then there is a

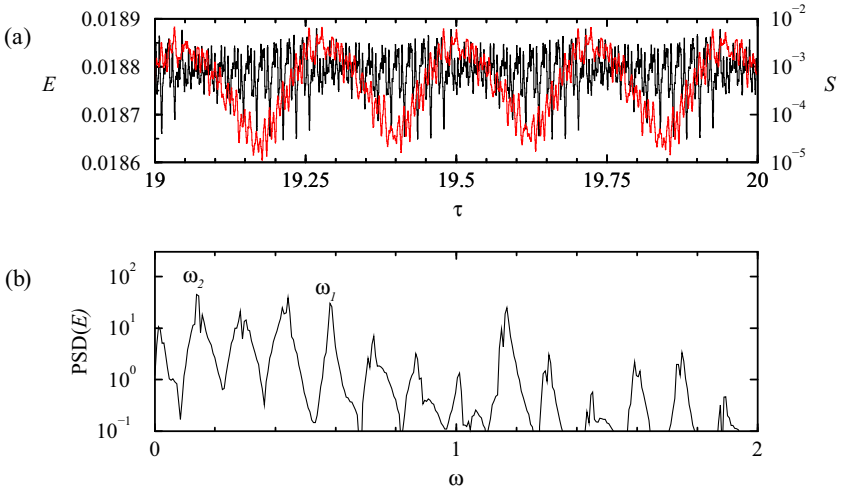

FIG. 7. (a) Time series of E (black) and S (red) for Re = 1980, zoomed in for a time during which the evolution is close to the mixed-mode QPa [with $\sigma(E) \approx 4 \times 10^{-5}$], and (b) power spectral density (PSD) of the time series of E shown in (a). The peaks corresponding to the frequencies of LC1 and LC2 are indicated.

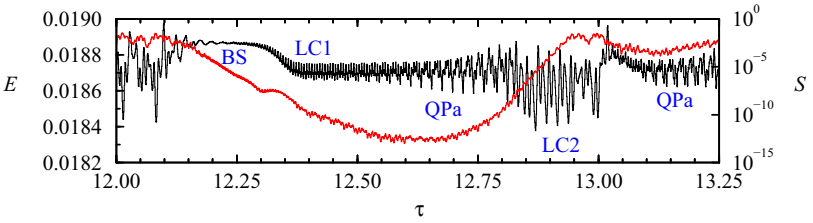

FIG. 8. Time series of E (black) and S (red) for $\mathrm{Re} = 2000$, zoomed in for a time during which there is a "regular" burst event.

another burst, but the evolution does not make it to the neighborhood of the BS this time and instead visits another quasiperiodic unstable state.

The limit cycle LC1 is symmetric, but is unstable to modulations, i.e., a Neimark-Sacker bifurcation, and the new frequency introduced is that of LC2. LC2 is unstable to symmetry breaking. For most of the time, the time series appears to be temporally chaotic, suggesting that the stable and unstable manifolds of the saddle states (BS, LC1, LC2, and QPa) intersect transversely, leading to chaotic dynamics interspersed with regular episodes during which the flow approaches sufficiently close to one or other saddle state, but eventually the dynamics are directed by the unstable manifolds. The mixed-mode QPa acts as a gateway in and out of the symmetric subspace and S grows and decays exponentially during the beat cycle. Further evidence supporting this is presented in the following sections where the flow is further analyzed.

C. Spectral analysis of the BS

Now that we have explored the dynamics as Re is increased beyond Re_{H1} via DNS and have reproduced the DNS results of previous investigations, we analyze the results. As was already done in [4], we begin by using SFD to obtain the unstable BS for $\mathrm{Re} > \mathrm{Re}_{H1}$ and then we determine its leading eigenmodes using Arnoldi iterations.

Figure 9 shows the real and imaginary parts of the three leading eigenvalue pairs as functions of Re. The leading eigenvalue pair (which we simply refer to as λ_1) acquires positive real part at $\mathrm{Re} \approx 1928.9$, which is consistent with the DNS results presented above. The imaginary part is approximately 0.5832 (using the convective time scale), which is very close to the oscillation frequency of LC1 and to the Hopf frequency reported in [4,5]. The second leading eigenpair λ_2 has a real part that is growing faster with Re than that of λ_1, but starting from a much more negative value. The real part of λ_2 becomes positive via a second Hopf bifurcation H_2 at $\mathrm{Re} = \mathrm{Re}_{H2} \approx 2089$. The imaginary part of λ_2 is approximately 0.1407, which is very close to the oscillation frequency of LC2. This value is also very close to the imaginary part of λ_2 reported by Loiseau *et al.* [4,5], however they did not consider the linear stability of the BS beyond $\mathrm{Re} = 2000$ and so they did not determine Re_{H2}. The eigenvectors associated with λ_1 and λ_2 are reflection symmetric. The third leading eigenvalue pair λ_3 has a real part that remains negative over the Re range considered and varies very slowly with Re, suggesting that if it is involved in a bifurcation of the BS, it would be at a much larger Re and so is not likely to have an impact on the dynamics at the Re values under consideration. It has an imaginary part slightly smaller than λ_1 and the associated eigenvector is antisymmetric. This is consistent with the findings of [4,5]. This is also consistent with the fact that this mode does not show up when the spectral analysis is done in the symmetric subspace.

D. Details of the subcritical Hopf bifurcation to LC1

Linear stability analysis identifies the onset of a bifurcation, but does not give information about whether it is super- or subcritical; that requires nonlinear information for its determination. Both [2] and [3] presented DNS evidence that the Hopf bifurcation H_1 at which the BS first loses stability is

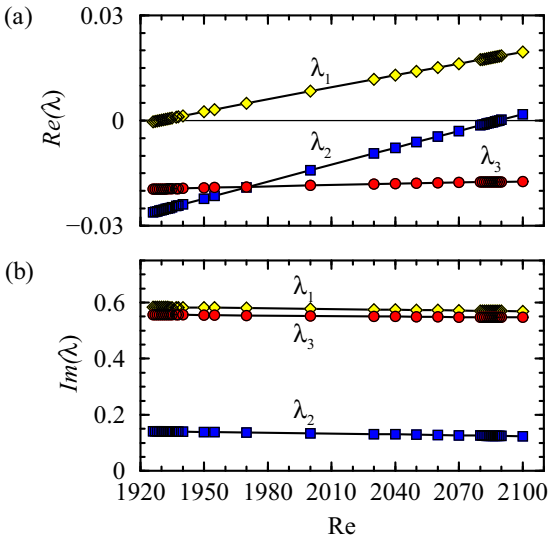

FIG. 9. Real and imaginary parts of the three leading eigenvalues of the BS as functions of Re, using the convective time scale.

subcritical. We now focus on the details of this subcritical Hopf bifurcation. The generic behavior in the neighborhood of a subcritical Hopf bifurcation is that the steady equilibrium (BS) loses stability at $\mathrm{Re} = \mathrm{Re}_{H1} \approx 1929 \pm 1$ and an unstable limit cycle (LC1) is spawned to lower Re. The next-order nonlinear terms in the normal form give that the unstable limit cycle undergoes a cyclic-fold bifurcation (also known as a saddle-node bifurcation of limit cycles) at $\mathrm{Re} = \mathrm{Re}_{CF1} < \mathrm{Re}_{H1}$. We have numerically determined (see below for details) $\mathrm{Re}_{CF1} \approx 1913.5 \pm 0.5$. For $\mathrm{Re} < \mathrm{Re}_{CF1}$ there are no limit cycles locally in phase space and for $\mathrm{Re} > \mathrm{Re}_{CF1}$ there are two limit cycles. One is the unstable lower-branch cycle that was spawned at the subcritical Hopf bifurcation and the other is a stable upper-branch cycle that continues to exist to higher Re (see [18], Chap. 8.2). The DNS results presented in the previous section, as well as those of [3–5], show that the upper-branch LC1 is unstable for $\mathrm{Re} \gtrsim \mathrm{Re}_{H1}$, but only very weakly so in the sense that there is a very long-lived transient that remains close to LC1 before bursting sets in.

The lower-branch LC1 is not directly accessible via DNS as it is unstable. However, by implementing the EST [9,10] using linear combinations of the upper-branch LC2 (which is stable in the symmetry subspace for $\mathrm{Re} \in [\mathrm{Re}_{CF1}, \mathrm{Re}_{H1}]$; see Sec. III E) and the BS as initial conditions, we have been able to obtain the unstable lower-branch LC1 as a long transient. A pair of transients at $\mathrm{Re} = 1916$ using $\alpha\mathrm{BS} + (1-\alpha)$(LC2 upper) as the initial condition, with $\alpha = 0.644442$ and $\alpha = 0.644443$, is shown in Fig. 10. With these two slightly different values of α, the transient remains close to the unstable lower-branch LC1 for about 1.5 viscous times, corresponding to about 270 oscillations, before the transient corresponding to the larger α evolves and converges to the BS, while the other transient converges to the upper-branch LC1. Close-ups of the oscillations corresponding to lower- and upper-branch LC1 are shown over 0.1 viscous times in Figs. 10(b) and 10(c); they both have approximately the same period and the upper-branch LC1 has larger amplitude and the form of its oscillation is more nonlinear. During the entire duration of these simulations, S remains at machine zero levels, indicating that the dynamics is occurring in the symmetry subspace.

By implementing the EST for $\mathrm{Re} \in [\mathrm{Re}_{CF1}, \mathrm{Re}_{H1}]$, we have been able to capture the lower-branch LC1. Figure 11 is a bifurcation diagram in the neighborhood of the subcritical Hopf bifurcation H_1, using the standard deviation in the energy oscillations $\sigma(E)$ as the state variable and Re as the bifurcation parameter. We use $\sigma(E)$ as a measure of the oscillation amplitude as the oscillations are

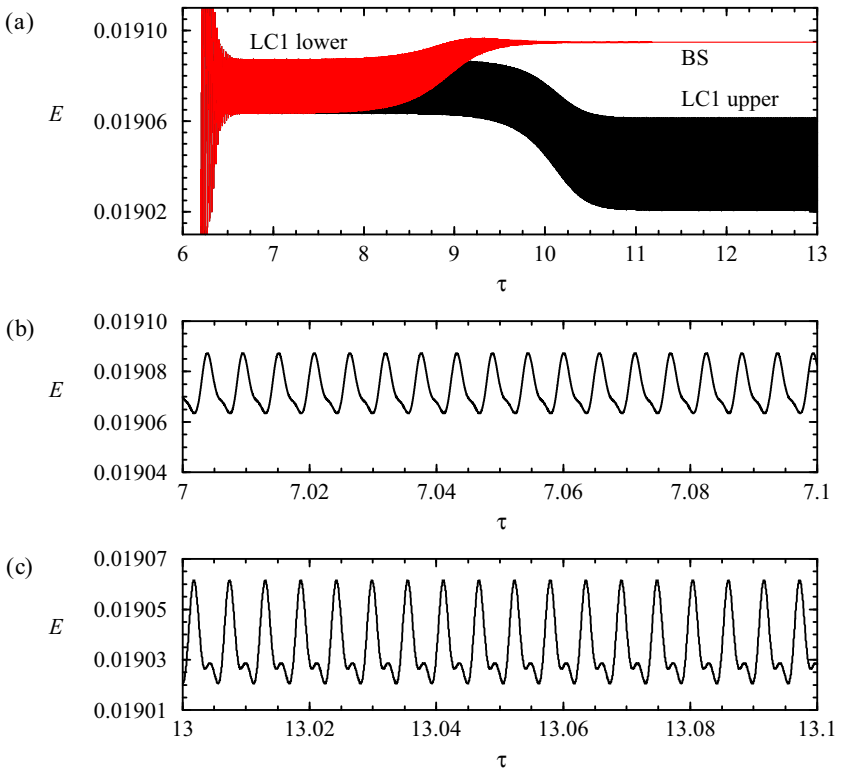

FIG. 10. Time series of E for EST simulations between the BS and upper-branch LC2 at $\mathrm{Re} = 1916$, showing (a) two transients using $\alpha\mathrm{BS} + (1-\alpha)$(LC2 upper) as the initial condition, with $\alpha = 0.644442$ (black, evolving to upper-branch LC1) and $\alpha = 0.644443$ (red, evolving to the BS). (b) Close-up of the time series for $\tau \in [7.0, 7.1]$ during which the transients are very close to lower-branch LC1. (c) Upper-branch LC1 oscillations for $\tau \in [13.0, 13.1]$.

far from harmonic, and so a peak-to-peak measure is not a good measure as it typically overestimates the average deviation away from the mean. Also shown is the cyclic-fold bifurcation CF_1 where the lower- and upper-branch LC1 meet at $\mathrm{Re}_{CF1} \approx 1913.5 \pm 0.5$. For $\mathrm{Re} < \mathrm{Re}_{H1}$, the BS is stable, and for $\mathrm{Re} > \mathrm{Re}_{H1}$, the BS loses stability acquiring one unstable (eigen)direction. Since the bifurcation is subcritical, with LC1 being spawned to lower Re, LC1 also has one unstable direction. At CF_1, LC1 folds from the lower to the upper branch and becomes stable (no unstable direction). We verified the stability of LC1 via DNS at $\mathrm{Re} = 1916$ for over 120 viscous time units, corresponding to over 20000 oscillations. LC1 loses stability in a Neimark-Sacker bifurcation NS_1 (a Hopf bifurcation of limit cycles) at $\mathrm{Re} = \mathrm{Re}_{NS1} \approx 1919 \pm 1$. For $\mathrm{Re} > \mathrm{Re}_{NS1}$, LC1 has one unstable direction. The details of how NS_1 is determined will be given below in Sec. III E, but briefly it involved using the EST with LC2 (stabilized in the symmetry subspace) and the BS. For some combinations, we found a long-lived transient with a quasiperiodic signature QPs. Figure 12 shows two such transients at $\mathrm{Re} = 1916$ that both stay close to QPs for over three viscous times and then one evolves toward LC2 and the other toward LC1. Also shown in the figure are the time series and corresponding power spectral density of E over a time interval when the flow is close to QPs. It is clear that QPs is a mixed mode of LC1 and LC2. Edge state technique simulations show that QPs exists for $\mathrm{Re} < \mathrm{Re}_{NS1}$, i.e., the Neimark-Sacker bifurcation of LC1 is subcritical, and so QPs has one unstable direction. More details are presented in Sec. III E. The important point here is that the upper-branch LC1 had to lose stability for the DNS results showing bursting (as in Fig. 2) to make

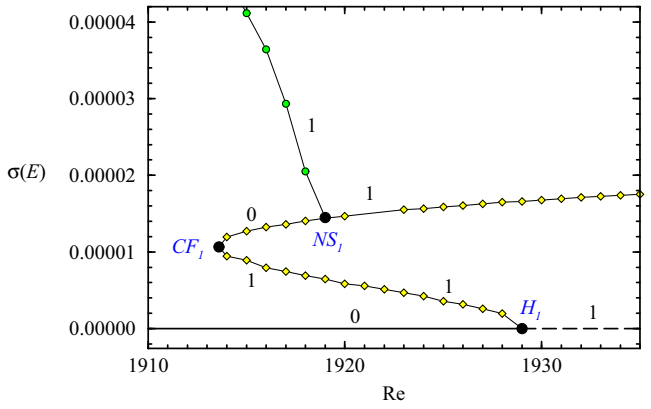

FIG. 11. Bifurcation diagram in the neighborhood of the subcritical Hopf bifurcation. The solid and dashed lines with $\sigma(E) = 0$ correspond to the BS, the curve with the yellow diamonds corresponds to LC1, and the curve with green circles corresponds to a mixed-mode between LC1 and LC2. The subcritical Hopf where the BS loses stability is labeled H_1, the cyclic-fold bifurcation between the lower and upper branches of LC1 is labeled CF_1, and the Neimark-Sacker bifurcation on the upper branch of LC1 is labeled NS_1. Along each equilibrium solution branch segment, there is an integer indicating the number of unstable directions associated with the equilibrium.

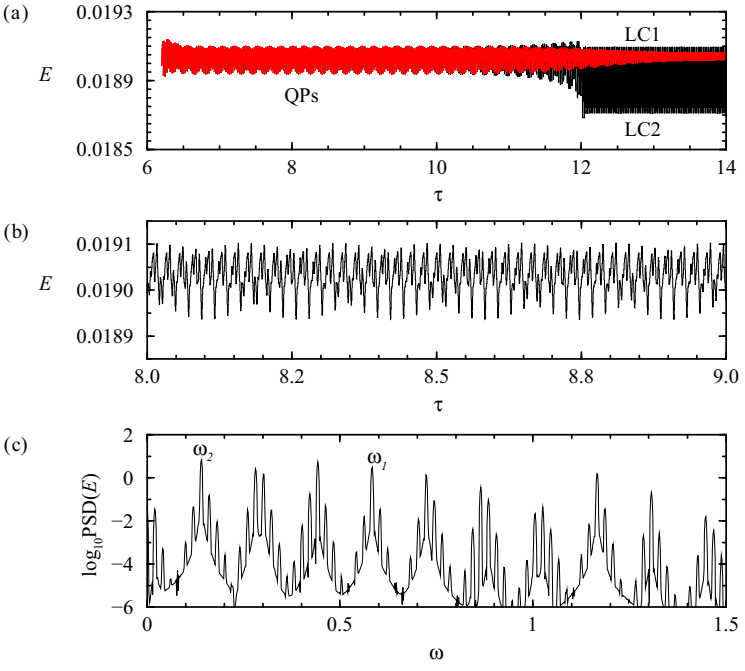

FIG. 12. Time series of E for EST simulations in the symmetry subspace between the BS and upper-branch LC2 at $\mathrm{Re} = 1916$, showing (a) two transients using $\alpha\mathrm{BS} + (1-\alpha)$(LC2 upper) as the initial condition, with $\alpha = 0.6294285$ (black, evolving to upper-branch LC2) and $\alpha = 0.6294286$ (red, evolving to upper-branch LC1). (b) Close-up of the time series for $\tau \in [8.0, 8.3]$ during which the transients are very close to QPs. (c) Power spectral density (PSD) of the time series of E over $\tau \in [7.0, 10.0]$.

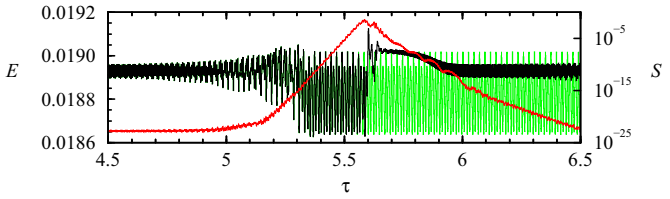

FIG. 13. Time series of E and S at Re = 1940. Shown are the same time series from Fig. 2(b), but zoomed in for $\tau \in [4.5,6.5]$ (black for E and red for S), as well as the time series starting with the same initial condition at $\tau = 0$, but computed in the symmetry subspace (only E is shown, in green, as $S = 0$ in the subspace).

sense. Note that the upper-branch LC1 is only stable over the range $\mathrm{Re}_{CF1} < \mathrm{Re} < \mathrm{Re}_{NS1}$, with $(\mathrm{Re}_{NS1} - \mathrm{Re}_{CF1})/(\mathrm{Re}_{NS1} + \mathrm{Re}_{CF1}) \approx 0.0014$, which is very small and easily missed; Refs. [3–5] do not report LC1 as being stable for any Re.

E. Dynamics in the symmetry subspace

The intermittent bursting behavior for $\mathrm{Re} \approx \mathrm{Re}_{H1}$, with the bursts correlated with large increases in the flow asymmetry, is a poorly understood feature of the onset of unsteadiness in the cubic lid-driven cavity [3–5]. In this section we explore the flow dynamics in the symmetry subspace in order to further investigate what dynamics are involved. Numerically, the flow is restricted to the subspace simply by setting $\boldsymbol{u} = 0.5[\boldsymbol{u} + \mathcal{A}(\mathcal{K})\boldsymbol{u}]$ at every time step (and intermediate time step) in the simulation.

Figure 13 shows a typical evolution in the subspace and compares it to that in the full space. The figure includes the time series from Fig. 2(b), cropped to $\tau \in [4.5,6.5]$ to focus on the first burst event. From Fig. 2(b) we saw that the flow stays very close to LC1 for over four viscous times before undergoing a burst. In Fig. 13 we now appreciate that the flow starts to depart from LC1 before there is any appreciable increase in its asymmetry, i.e., S does not start to grow until $\tau \approx 4.9$, but by $\tau = 4.6$ there is a significant departure from the periodic signal associated with LC1 due to a modulation. This modulation is due to the Neimark-Sacker bifurcation NS_1 at which QPs is spawned. By $\tau \approx 5.2$, QPs is large and becomes irregular while S is growing exponentially. There is a rapid adjustment in the flow and by $\tau \approx 5.4$, the flow transient approaches close to LC2. During this time, S is still small, but continues to grow exponentially. Over this same period of time, the evolution in the symmetric subspace is virtually identical (except, of course, that $S = 0$). This is clear evidence that the transition from LC1 to LC2 via modulation is not due to symmetry breaking; LC1 is unstable in the subspace, as is the BS at this Re, and there is an eventual evolution to LC2 that is virtually identical to that in the full space.

The evolution in the subspace converges onto LC2 at $\tau \approx 5.4$ and remains at LC2 indefinitely. In the full space, LC2 is unstable to symmetry breaking. By $\tau \approx 5.55$, there is an appreciable difference between the kinetic energy of LC2 in the full space and that in the subspace. As S saturates at $\tau \approx 5.6$, the evolution quickly evolves away from the unstable LC2, briefly approaches the unstable BS, which nevertheless is symmetric, and so during the approach to the BS S decays exponentially. Since the BS is unstable, the evolution ends up tracking an unstable manifold away from the BS and approaches LC1. In the full space (at Re = 1940 under consideration) LC1 is unstable and like the BS it too is symmetric. Hence, while the evolution is in the neighborhood of LC1, S continues to decay exponentially, albeit at a different rate. LC1 becomes modulated by $\tau \approx 6.2$, but this modulation is also symmetric and S continues to decay exponentially. As the modulation amplitude grows, another burst is initiated, as shown in Fig. 2(b). So, in summary, we have for $\mathrm{Re} \gtrsim 1930$ that both the BS and LC1 are unstable but symmetric and LC2 is stable in the subspace, but unstable to symmetry breaking.

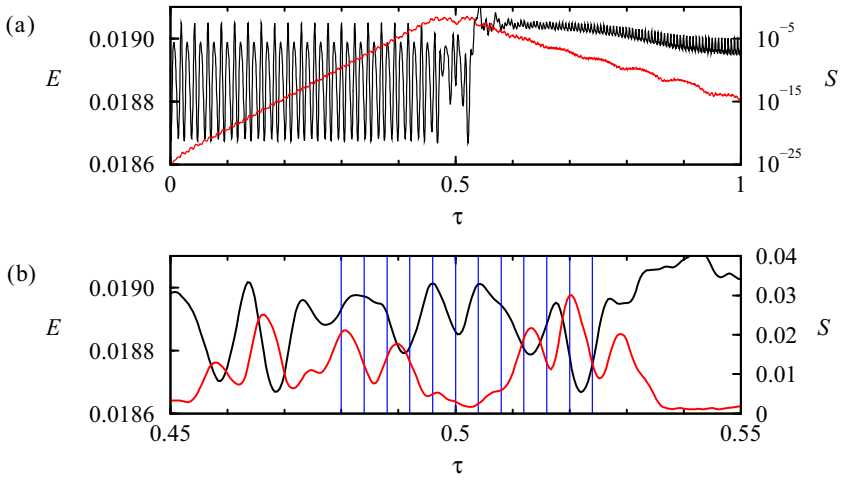

FIG. 14. Time series of E (black) and S (red) for Re = 1930. (b) Close-up of (a) near $\tau = 0.5$; the vertical blue lines correspond to the times of the snapshots shown in Fig. 15.

It is now interesting to examine the symmetry breaking of LC2 in the full space. To do this, we have first computed LC2 in the subspace at Re = 1930 and used that solution as the initial condition for a simulation in the full space at the same Re = 1930. Figure 14(a) shows the evolutions of E and S in this simulation. Initially, S is at machine ϵ^2 and grows exponentially. During this early part of the evolution, the flow essentially corresponds to the LC2 state that is stable in the subspace, until $\tau \approx 0.5$, by which time S has grown to $\sim 10^{-3}$ and a bursting event very similar to those shown in Fig. 2(a) is initiated. Figure 14(b) is a close-up of the evolution shown in Fig. 14(a), covering the duration of the burst when S is maximal and just as the flow transitions toward LC1 and S decays exponentially. The 12 vertical (blue) lines in the figure correspond to snapshots of the helicity isosurfaces shown in Fig. 15. Note that these isosurfaces are of the full solution, in contrast to those shown in Figs. 4 and 5, which showed helicity isosurfaces of the deviation away from the mean; during the bursting event, there is no meaningful mean. As such, the isosurfaces include the contribution from the spanwise end-wall regions. The nature of the flow is difficult to discern

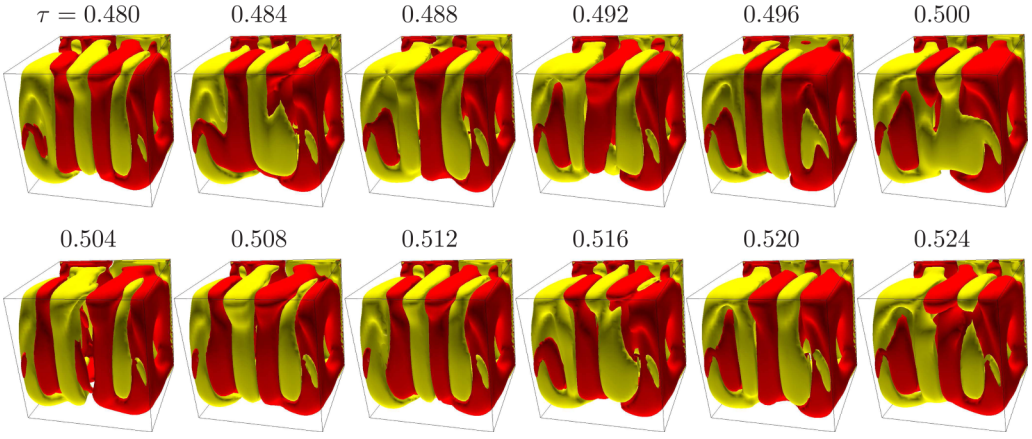

FIG. 15. Helicity isosurfaces at $\mathcal{H} = \pm 10^5$ for Re = 1930 during the transition from LC2 at times indicated by the blue vertical lines in Fig. 14(b). See movie 3 in the Supplemental Material [17] for an animation from $\tau = 0.344$ to 0.664.

from the 12 snapshots, but the corresponding online movie 3 in [17] is very insightful. The movie starts at $\tau = 0.344$ when the flow is very near LC2 and consists of waves traveling symmetrically in from the two spanwise end walls and annihilating at the midplane, i.e., the typical LC2 behavior described earlier. Then, in the transitional stage with $\tau \in (4.8,5.2)$, during which S has saturated, the flow consists of waves traveling from one spanwise end wall to the other. This traveling wave (TW) is very unstable and only lasts for about one and a half cycles, but it is clearly discernible in the movie. In principle, both left- and right-traveling waves are possible and which is observed depends on the details of the symmetry-breaking perturbation at the time. The instability of the TW is likely due to confinement effects in the cubic cavity. Such traveling-wave states have been observed experimentally in an oscillatory lid-driven cavity of large spanwise extent [19] and are related to the symmetry-breaking dynamics in the spanwise periodic idealization of that flow [20–22]. Following the instability of the TW, the movie shows a rapid transition to oscillations that are converging toward LC1.

The differences between the evolutions in the full space and in the subspace for $\mathrm{Re} < \mathrm{Re}_{H1} \approx 1929$ also provide significant insight into the dynamics involved. As mentioned in the previous section, evolutions for $\mathrm{Re} \lesssim 1930$ in the full space eventually converge onto the stable BS, independently of initial conditions, as the BS is the only stable state at these Re, except for $\mathrm{Re}_{CF1} < \mathrm{Re} < \mathrm{Re}_{NS1}$, an interval of only six units in Re ($[\mathrm{Re}_{NS1} - \mathrm{Re}_{CF1}]/[\mathrm{Re}_{NS1} + \mathrm{Re}_{CF1}] \approx 0.0014$), over which LC1 is also stable. In the subspace however, LC2 is stable down to $\mathrm{Re} = \mathrm{Re}_{CF2} \approx 1872$, where it undergoes a cyclic-fold bifurcation CF_2 and does not exist for lower Re, leaving the BS as the only stable state for $\mathrm{Re} < \mathrm{Re}_{CF2} \approx 1871.5 \pm 0.5$.

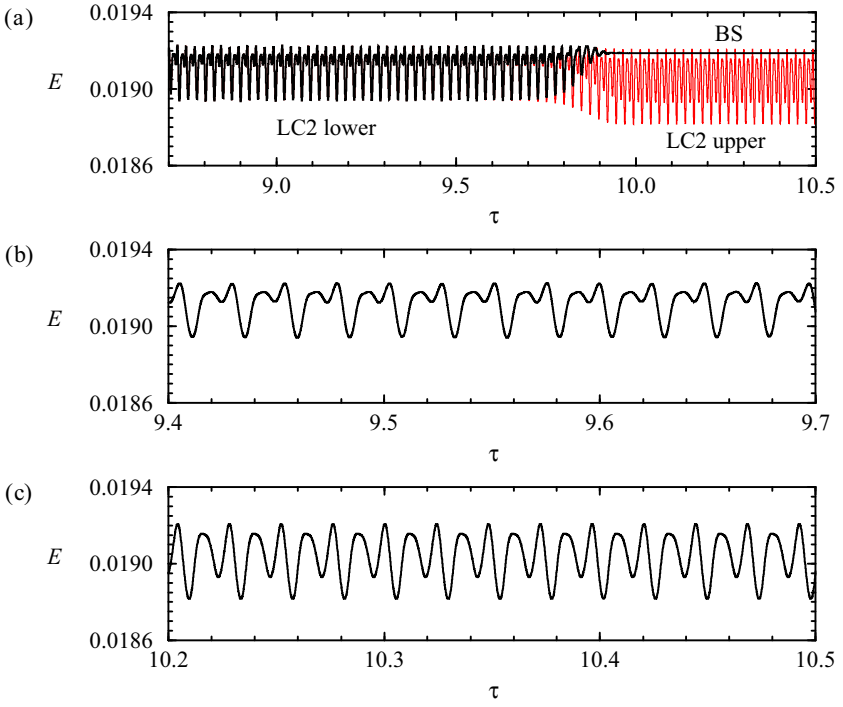

FIG. 16. Time series of E for the EST simulation in the symmetric subspace between the BS and upper-branch LC2 at $\mathrm{Re} = 1883$, showing (a) two transients using $\alpha\mathrm{BS} + (1-\alpha)$(LC2 upper) as the initial condition, with $\alpha = 0.39042645732$ (black, evolving to the BS) and $\alpha = 0.39042645730$ (red, evolving to upper-branch LC2). (b) Close-up of the time series for $\tau \in [9.4,9.7]$ during which the transients are very close to lower-branch LC2. (c) Upper-branch LC2 oscillations for $\tau \in [10.2,10.5]$.

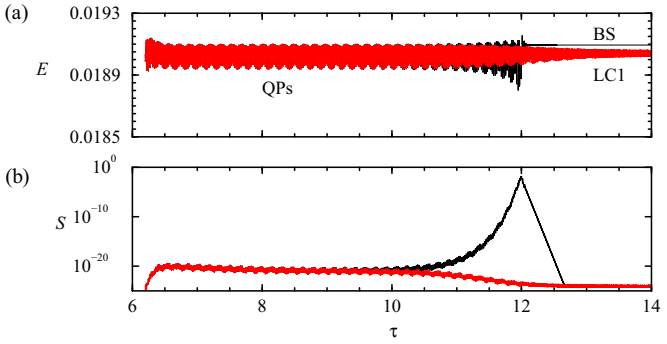

FIG. 17. Time series of (a) E and (b) S for EST simulations at $\mathrm{Re} = 1916$, showing two transients using $\alpha\mathrm{BS} + (1-\alpha)$(LC2 upper) as the initial condition, with $\alpha = 0.6294285$ (black, evolving to the BS) and $\alpha = 0.6294286$ (red, evolving to upper-branch LC1). These EST runs are the same as those shown in Fig. 12, but executed in the full space.

For $\mathrm{Re} \gtrsim \mathrm{Re}_{CF2}$, we have implemented the EST in the symmetry subspace, using linear combinations of the BS and LC2 in order to localize the lower-branch LC2 involved in the cyclic-fold bifurcation CF_2. In the subspace, near the cyclic-fold bifurcation, the lower-branch LC2 is a saddle limit cycle with one unstable direction. Figure 16 shows time series of E for a pair of EST simulations in the subspace at $\mathrm{Re} = 1883$, where the initial conditions were $(\alpha)\mathrm{BS} + (1-\alpha)$(LC2 upper) with $\alpha = 0.390\,426\,457\,32$ that ended up evolving to the BS and $\alpha = 0.390\,426\,457\,30$ that ended up evolving to upper-branch LC2. With these choices of α, the evolutions remain very close to the saddle lower-branch LC2 for about one viscous time; Fig. 16(b) is a close-up of the E time series over $\tau \in [9.4, 9.7]$ to more clearly see the oscillations of lower-branch LC2. From this we have extracted the standard deviation of the oscillation $\sigma(E)$ and the corresponding frequency. Figure 16(c) is a close-up over $\tau \in [10.2, 10.5]$ of the time series that evolves to LC2. We have made movies of these two oscillations (not shown) and they are essentially the same as the one associated with upper-branch LC2 in Fig. 5.

The identification of the unstable lower-branch LC2 emanating from CF_2 is relatively straightforward because in the symmetry subspace its unstable manifold is only one-dimensional and can parametrized by α: Lower-branch LC2 is the edge state between upper-branch LC2 and the BS, corresponding to a single value of α. With deviations only in the 11th significant figure away from this value of α, we obtain transients that remain very close to lower-branch LC2 for more than one viscous time. Larger deviations in α reduce this time considerably. Repeating the EST simulations to higher Re also reduces the time spent near lower-branch LC2 for the same level of refinement in α. For $\mathrm{Re} \gtrsim 1886$, EST simulations with refinements of α to different values lead to long transients close to either lower-branch LC2, much as been just described, or to QPs as illustrated in Fig. 12 for $\mathrm{Re} = 1916$. This indicates that lower-branch LC2 undergoes a Neimark-Sacker bifurcation NS_2 (by doing several EST simulations at many Re, we estimate this to occur at $\mathrm{Re} = \mathrm{Re}_{NS2} \approx 1886 \pm 3$), spawning the mixed-mode QPs supercritically (i.e., to larger Re). The supercriticality of NS_2 means that lower-branch LC2 acquires another unstable direction for $\mathrm{Re} > \mathrm{Re}_{NS2}$, totaling two in the symmetry subspace, and QPs has the same number of unstable directions as the lower-branch LC2 from which it bifurcates, namely, one. Having only one unstable direction, QPs was tracked via the EST all the way to NS_1, where it is absorbed by upper-branch LC1 (see Fig. 11 and the accompanying text for details). For lower-branch LC2, having two unstable directions for $\mathrm{Re} > \mathrm{Re}_{NS2}$ means that localizing it using bisection in α is no longer possible. We have been able to localize lower-branch LC2 up to $\mathrm{Re} = 1914$, but for larger Re a different strategy is needed.

The evolution of E and S in the full space at $\mathrm{Re} = 1916$ when started from QPs, which is now unstable in at least two directions, is shown in Fig. 17. In addition to the unstable direction in the

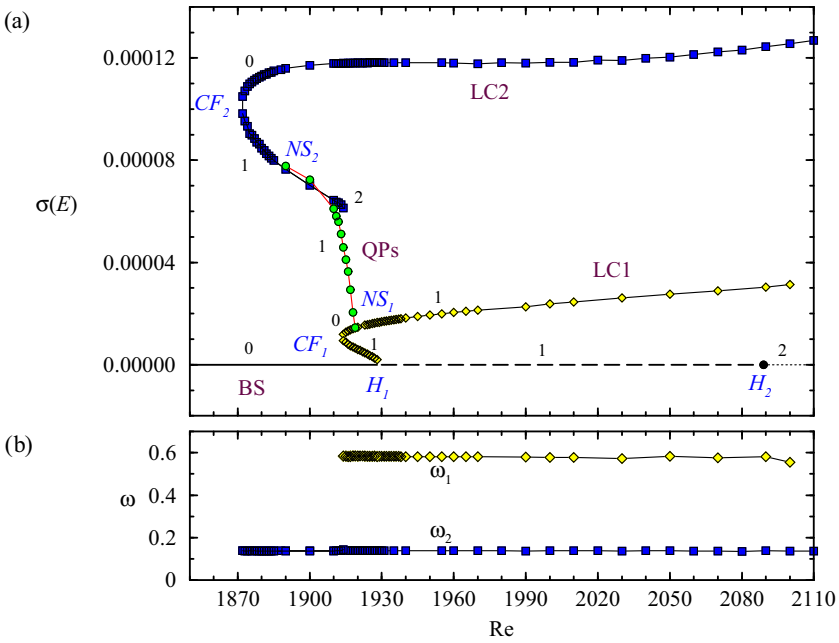

FIG. 18. Variation with Re of (a) the oscillation amplitudes $\sigma(E)$ of the various states as indicated, with the integer indicating the number of unstable directions associated with each state (unstable states were found by restriction to the symmetry subspace, SFD, or EST), and (b) the frequencies ω_1 and ω_2 of LC1 (diamonds) and LC2 (squares). Note that the frequencies of the upper and lower branches of each are virtually the same. The critical Re for the various bifurcations indicated are listed in Table I.

symmetry subspace, QPs now has an additional unstable direction out of the subspace, illustrated by the growth of S associated with the smaller value of α. For that initial condition, QPs loses stability via symmetry breaking and the dynamics eventually visits the basin of attraction of the BS, while the state originating from an initial condition associated with the slightly larger α remains symmetric and evolves toward LC1, which is the only other stable state in the full space at this Re besides the BS. The similarity in spectral signatures between QPs in Fig. 12 and QPa in Fig. 7 obtained at a slightly lower Re suggests that the symmetry breaking of QPs indeed results in QPa (a pair of them, related by the reflection).

F. Summary of identified states

All the information acquired using the various numerical techniques is used to construct Fig. 18, showing the standard deviation in the kinetic energy $\sigma(E)$ and the oscillation frequency ω of the states found. Table 1 provides the critical Re for the bifurcations involved. A brief overview of the various states in Fig. 18, how they were found, and their stability properties that we have been able to educe now follows.

(i) BS. The basic state, by definition, is symmetric. It first loses stability at $\mathrm{Re} = \mathrm{Re}_{H1}$ in a subcritical Hopf bifurcation H_1 and then suffers a second Hopf bifurcation H_2 at $\mathrm{Re} = \mathrm{Re}_{H2}$. The unstable BS was computed via SFD and the bifurcations were identified using Arnoldi iterations.

(ii) LC1. This limit cycle is spawned from the BS at H_1 subcritically toward lower Re. At onset, it has one unstable direction. It undergoes a cyclic-fold bifurcation CF_1 at $\mathrm{Re} = \mathrm{Re}_{CF1}$, where it (the lower branch) is folded to continue to higher Re (the upper branch). The upper branch is stable for $\mathrm{Re} \in (\mathrm{Re}_{CF1}, \mathrm{Re}_{NS1})$; at Re_{NS1} it undergoes a Neimark-Sacker bifurcation and for $\mathrm{Re} > \mathrm{Re}_{NS1}$, LC1 has one unstable direction. Even though it is unstable, the growth rate of small perturbations

TABLE I. List of bifurcations encountered and the critical Re at which they occur.

Bifurcation	Re
H_1, first Hopf of the BS	1929 ± 1
H_2, second Hopf of the BS	2089 ± 1
CF_1, cyclic-fold of LC1	1913.5 ± 0.5
CF_2, cyclic-fold of LC2	1871.5 ± 0.5
NS_1, Neimark-Sacker of LC1 (upper branch)	1919 ± 1
NS_2, Neimark-Sacker of LC2 (lower branch)	1886 ± 3

away from it is very slow and its characteristics can be determined via DNS with initial conditions that are reasonably close to LC1. The lower-branch LC1 was computed using the EST with linear combinations of the BS and upper-branch LC2 as well as linear combinations of the BS and upper-branch LC1. The LC1 (both lower and upper branches) are stable to symmetry breaking; this was determined by monitoring S during simulations.

(iii) LC2. This limit cycle was first found by restricting DNS to the symmetric subspace. For $\mathrm{Re} > \mathrm{Re}_{H1}$, there are no stable steady or time-periodic solutions in the full space, but in the subspace any initial condition evolves to LC2. LC2 was continued down to $\mathrm{Re} = \mathrm{Re}_{CF2}$ where it undergoes a cyclic-fold bifurcation CF_2 and is folded to form lower-branch LC2, which has one unstable direction in the subspace for $\mathrm{Re} \in (\mathrm{Re}_{CF2}, \mathrm{Re}_{NS2})$. This lower-branch LC2 was computed using the EST in the subspace with combinations of the BS and upper-branch LC2 as initial conditions. Direct numerical simulations in the full space with LC2 (upper and lower) as initial conditions show that LC2 is unstable to symmetry breaking. An example of such a DNS at $\mathrm{Re} = 1883$ is shown in Fig. 19. The initial condition used was close to lower-branch LC2. The figure shows exponential growth in S while the trajectory is near LC2. For $\mathrm{Re} > \mathrm{Re}_{NS2}$, lower-branch LC2 in the subspace has two unstable directions and we were not able to continue it very far using the EST. However, it is a reasonable conjecture that it continues until it meets the BS at H_2, given the similarities in the spatiotemporal structure of lower- and upper-branch LC2 and the eigenfunction that bifurcates at H_2 (see the next section for supporting arguments).

(iv) QPs. For $\mathrm{Re} \in (\mathrm{Re}_{NS2}, \mathrm{Re}_{NS1})$ there is a symmetric quasiperiodic state that is a mixed mode of LC1 and LC2. It was found using EST using certain combinations of the BS and LC2 as initial conditions in the symmetric subspace. As is typical of quasiperiodic mixed modes, it is spawned at a Neimark-Sacker bifurcation of one limit cycle (NS_2 on lower-branch LC2) and terminates at another Neimark-Sacker bifurcation of the other limit cycle (NS_1 on upper-branch LC1). QPs in the subspace has one unstable direction. Direct numerical simulations in the full space using QPs as the initial condition show that it also has an unstable direction out of the subspace. This indicates that a pitchfork bifurcation of QPs would spawn a pair of symmetry-related mixed modes in the full space, QPa. QPa would have (at least) two unstable directions. We have seen glimpses of QPa, for example, at $\mathrm{Re} = 1980$ (see Fig. 7) and $\mathrm{Re} = 2000$ (see Fig. 8).

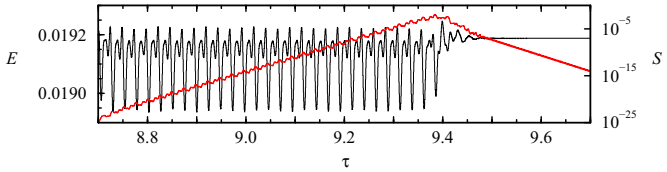

FIG. 19. Time series of E (black) and S (red) starting from the EST-determined lower-branch LC2 [using $\alpha\mathrm{BS} + (1-\alpha)$(LC2 upper) as the initial condition, with $\alpha = 0.390\,426\,457\,30$], but evolving in the full space, at $\mathrm{Re} = 1883$.

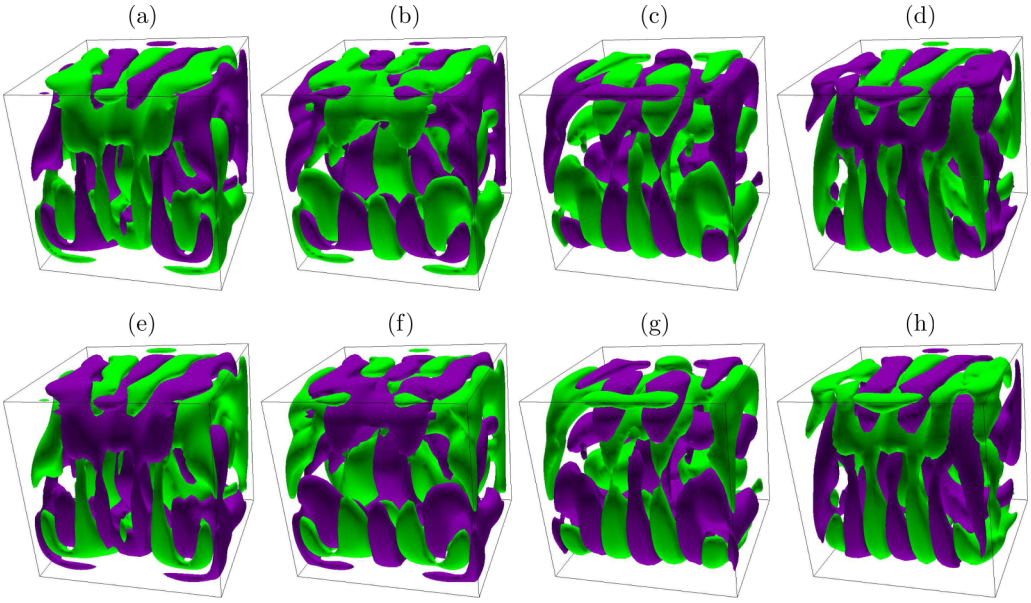

FIG. 20. Isosurfaces of the y component of $\mathbf{\Phi}$ at Re $= 2090$. The isosurfaces (green is positive and purple is negative) are at $\pm 15\%$ of the maximum over one period. See movie 4 in the Supplemental Material [17] for an animation. (a) $t = 0$, (b) $T/8$, (c) $2T/8$, (d) $3T/8$, (e) $4T/8$, (f) $5T/8$, (g) $6T/8$, and (h) $7T/8$.

G. Connection between LC2 and H_2

The picture summarized in the preceding section is fairly complete albeit missing some pieces, specifically the possible connection between the lower-branch LC2 and the second Hopf bifurcation H_2. As already noted in [4,5] and confirmed by our own analysis in Sec. III C, the Hopf frequency is very close to the oscillation frequency of LC2, suggesting that LC2 is the limit cycle that bifurcates from the BS at H_2. To further support this conjecture, we compare the spatiotemporal structure of LC2 with that of the eigenfunction corresponding to λ_2. Figure 20 shows the spatiotemporal dynamics of the y component of the real part of the rotated eigenmode $\mathbf{\Phi_2}$ associated with $\lambda_2 = \rho + i\omega$,

$$\mathbf{\Phi}(x,y,z,t) = \mathrm{Re}(\mathbf{\Phi}_2)\cos(\omega t) + \mathrm{Im}(\mathbf{\Phi}_2)\sin(\omega t). \tag{8}$$

The resulting cycle consists of waves coming in symmetrically from lateral walls meeting at the midplane. For comparison purposes, the isosurface of $v - \langle v \rangle$ of upper-branch LC2 at Re $= 2090$ is shown in Fig. 21 and exhibits the same type of spatiotemporal behavior. The comparison is even clear from the two corresponding online movies 4 and 5 in [17]. Figure. 22 shows the isosurfaces of $\mathcal{H} - \langle \mathcal{H} \rangle$ of upper-branch LC2 at Re $= 2090$, which are very similar to those at Re $= 1930$ shown in Fig. 5 and the accompanying online movies.

IV. DISCUSSION AND CONCLUSIONS

Symmetries and symmetry-breaking bifurcations play an important role in canonical flows, often leading to spatiotemporal chaos in the neighborhood of primary instabilities, and may be intricately involved in the transition to turbulence. The lid-driven cavity is one such canonical flow and recent explorations of the onset of unsteadiness in the cubic cavity have revealed that it comes in the form of bursts at irregular time intervals. With careful consideration of the symmetries of the problem and comparing the flows in the full space and in the symmetric subspace, we have shown that the bursts are excursions away from and back toward the symmetric subspace. These excursions are trajectories in phase space shadowing the stable and unstable manifolds of several saddle states

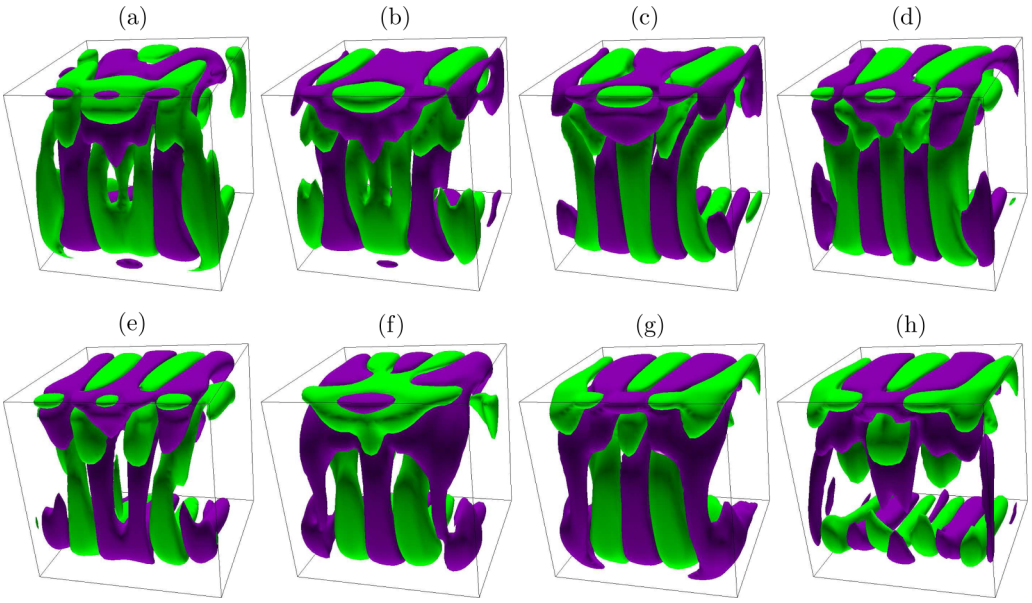

FIG. 21. Isosurfaces of $v - \langle v \rangle$ at ± 30 at $\mathrm{Re} = 2090$ (green is negative and purple is positive). See movie 5 in the Supplemental Material [17] for an animation. (a) $t = 0$, (b) $T/8$, (c) $2T/8$, (d) $3T/8$, (e) $4T/8$, (f) $5T/8$, (g) $6T/8$, and (h) $7T/8$.

that result following two successive Hopf bifurcations of the basic state as the Reynolds number is increased. Similar complicated dynamics associated with symmetry-breaking bifurcations in a very small neighborhood of parameter space, resulting in slow drifts from one saddle state to another,

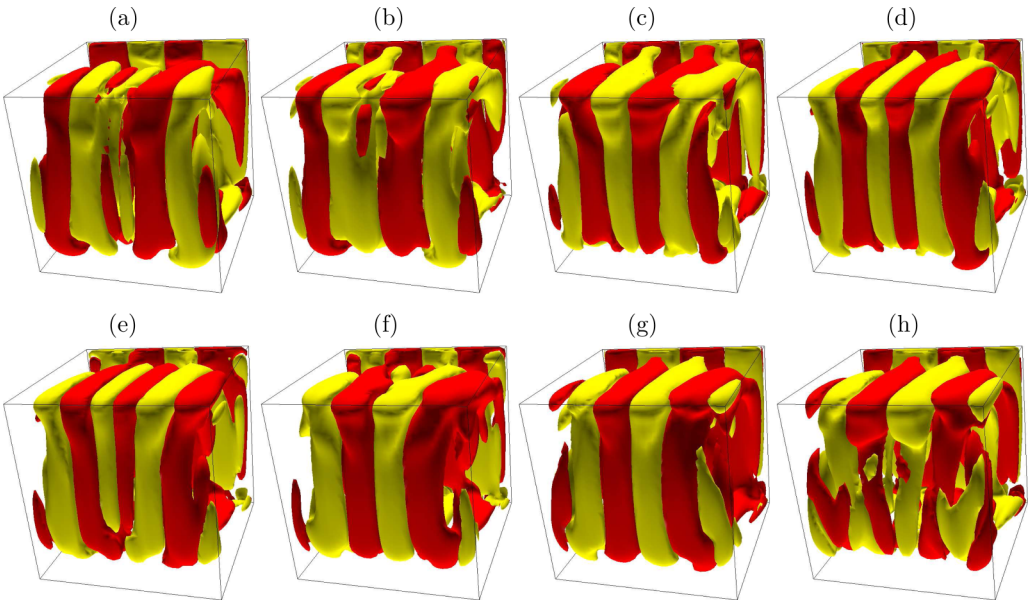

FIG. 22. Isosurfaces of $\mathcal{H} - \langle \mathcal{H} \rangle$ at $\pm 10^5$ at $\mathrm{Re} = 2090$ (yellow is negative and red is positive). See movie 6 in the Supplemental Material [17] for an animation. (a) $t = 0$, (b) $T/8$, (c) $2T/8$, (d) $3T/8$, (e) $4T/8$, (f) $5T/8$, (g) $6T/8$, and (h) $7T/8$.

have been studied in other canonical flows, such as small aspect-ratio Taylor-Couette flow [23–27] and precessing cylinder flow [28,29].

Our simulations, both in the full space and in the symmetric subspace, strongly indicate that the onset of unsteadiness in the cubic lid-driven cavity is organized by two successive subcritical Hopf bifurcations of the base state. The two Re at which these occur differ by about 8%. This can lead to the type of intermittency that has been reported; the other ingredient needed in order to rationalize the observation is the breaking of the spanwise reflection symmetry. The subcritical nature of the first Hopf bifurcation along with the symmetry breaking results in all steady, periodic, and quasiperiodic states being unstable local saddle states with a very small number of unstable manifolds in the full space for Re beyond the first bifurcation of the basic state. The lack of any local attractors often leads to intermittent chaotic behavior, with chaotic bursts resulting from repeated divergence away from the (weakly) repelling steady, periodic, or quasiperiodic state, alternating with nearly periodic phases as the trajectory is reinjected into the vicinity of the weakly unstable local states. However, in the symmetric subspace LC2 is stable and the intermittent bursting is not present.

ACKNOWLEDGMENTS

This work was partially supported by National Science Foundation Grant No. CBET-1336410. The computations were performed on the Saguaro Cluster of ASU Research Computing and School of Mathematical and Statistical Sciences computing facilities.

[1] P. N. Shankar and M. D. Deshpande, Fluid mechanics in the driven cavity, Annu. Rev. Fluid Mech. **32**, 93 (2000).

[2] Y. Feldman and A. Y. Gelfgat, Oscillatory instability of a three-dimensional lid-driven flow in a cube, Phys. Fluids **22**, 093602 (2010).

[3] H. C. Kuhlmann and S. Albensoeder, Stability of the steady three-dimensional lid-driven flow in a cube and the supercritical flow dynamics, Phys. Fluids **26**, 024104 (2014).

[4] J.-C. Loiseau, Dynamics and global analyses of three-dimensional flows, Ph.D. thesis, Paris Institute of Technology, 2014.

[5] J.-C. Loiseau, J.-C. Robinet, and E. Leriche, Intermittency and transition to chaos in the cubical lid-driven cavity flow, Fluid Dyn. Res. **48**, 061421 (2016).

[6] A. Liberzon, Y. Feldman, and A. Y. Gelfgat, Experimental observation of the steady-oscillatory transition in a cubic lid-driven cavity, Phys. Fluids **23**, 084106 (2011).

[7] E. Åkervik, L. Brandt, D. S. Henningson, J. Hœpffner, O. Marxen, and P. Schlatter, Steady solutions of the Navier-Stokes equations by selective frequency damping, Phys. Fluids **18**, 068102 (2006).

[8] Y. Saad, *Numerical Methods for Large Eigenvalue Problems*, 2nd ed. (SIAM, Philadelphia, 2011).

[9] T. Itano and S. Toh, The dynamics of bursting process in wall turbulence, J. Phys. Soc. Jpn. **70**, 703 (2001).

[10] T. M. Schneider, J. F. Gibson, M. Lagha, F. De Lillo, and B. Eckhardt, Laminar-turbulent boundary in plane Couette flow, Phys. Rev. E **78**, 037301 (2008).

[11] S. Hugues and A. Randriamampianina, An improved projection scheme applied to pseudospectral methods for the incompressible Navier-Stokes equations, Int. J. Numer. Methods Fluids **28**, 501 (1998).

[12] J.-M. Vanel, R. Peyret, and P. Bontoux, in *Numerical Methods for Fluid Dynamics II*, edited by K. W. Morton and M. J. Baines (Clarendon, Oxford, 1986), pp. 463–475.

[13] J. M. Lopez and J. Shen, An efficient spectral-projection method for the Navier-Stokes equations in cylindrical geometries I. Axisymmetric cases, J. Comput. Phys. **139**, 308 (1998).

[14] J. P. Boyd, *Chebyshev and Fourier Spectral Methods*, 2nd ed. (Dover, New York, 2001).

[15] L. S. Tuckerman and D. Barkley, in *Numerical Methods for Bifurcation Problems and Large-Scale Dynamical Systems*, edited by E. Doedel and L. S. Tuckerman, The IMA Volumes in Mathematics and its Applications Vol. 119 (Springer, Berlin, 2000), pp. 453–466.

[16] F. Gómez, R. Gómez, and V. Theofilis, On three-dimensional global linear instability analysis of flows with standard aerodynamics codes, Aerosp. Sci. Technol. **32**, 223 (2014).
[17] See Supplemental Material at http://link.aps.org/supplemental/10.1103/PhysRevFluids.2.074401 for animations corresponding to Figs. 4, 5, 15, and 20–22.
[18] S. H. Strogatz, *Nonlinear Dynamics and Chaos*, 2nd ed. (Addison-Wesley, Reading, 2015).
[19] J. J. F. Leung, A. H. Hirsa, H. M. Blackburn, F. Marques, and J. M. Lopez, Three-dimensional modes in a periodically driven elongated cavity, Phys. Rev. E **71**, 026305 (2005).
[20] H. M. Blackburn and J. M. Lopez, The onset of three-dimensional standing and modulated traveling waves in a periodically driven cavity flow, J. Fluid Mech. **497**, 289 (2003).
[21] F. Marques, J. M. Lopez, and H. M. Blackburn, Bifurcations in systems with Z_2 spatio-temporal and $O(2)$ spatial symmetry, Physica D **189**, 247 (2004).
[22] H. M. Blackburn, F. Marques, and J. M. Lopez, Symmetry breaking of two-dimensional time-periodic wakes, J. Fluid Mech. **522**, 395 (2005).
[23] J. M. Lopez and F. Marques, Small aspect ratio Taylor-Couette flow: Onset of a very-low-frequency three-torus state, Phys. Rev. E **68**, 036302 (2003).
[24] J. M. Lopez and F. Marques, Finite aspect ratio Taylor-Couette flow: Shil'nikov dynamics of 2-tori, Physica D **211**, 168 (2005).
[25] J. Abshagen, J. M. Lopez, F. Marques, and G. Pfister, Symmetry Breaking Via Global Bifurcations of Modulated Rotating Waves in Hydrodynamics, Phys. Rev. Lett. **94**, 074501 (2005).
[26] F. Marques and J. M. Lopez, Onset of three-dimensional unsteady states in small aspect-ratio Taylor-Couette flow, J. Fluid Mech. **561**, 255 (2006).
[27] J. Abshagen, J. M. Lopez, F. Marques, and G. Pfister, Bursting dynamics due to a homoclinic cascade in Taylor-Couette flow, J. Fluid Mech. **613**, 357 (2008).
[28] F. Marques and J. M. Lopez, Precession of a rapidly rotating cylinder flow: Traverse through resonance, J. Fluid Mech. **782**, 63 (2015).
[29] J. M. Lopez and F. Marques, Nonlinear and detuning effects of the nutation angle in precessionally-forced rotating cylinder flow, Phys. Rev. Fluids **1**, 023602 (2016).